SUPPLEMENTARY FIGURES

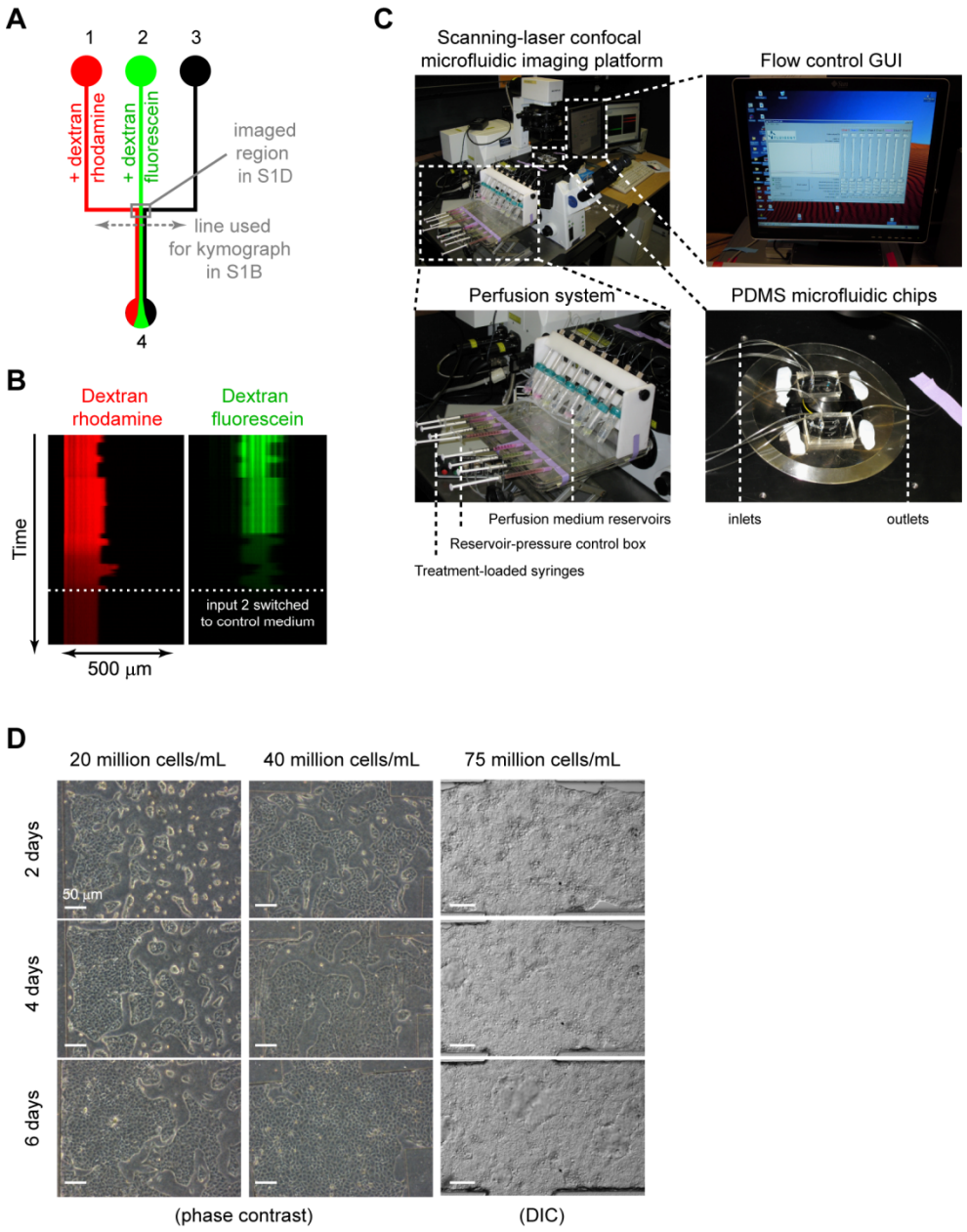

Supplementary Figure S1. Optimization of the microfluidic platform and cell growth conditions in chip. (**A**) Original chip geometry used to test flow control systems. Inlet 1 is loaded with a fluorescent dextran rhodamine solution (red) and inlet 2 with a fluorescent dextran fluorescein solution (green), while inlet 3 does not contain any dye and 4 is the outlet. (**B**) Kymograph of the streams labeled with fluorescent dyes as metioned in A, upon perfusion with a modified microinjection system. Frequent and prolonged oscillations compromise the precision of the treatment. (**C**) Photographs of the chosen confocal imaging and microfluidic platform. In this experiment two chips were simultaneously perfused and reservoir content could be adjusted using loaded syringes while imaging and without affecting flow positioning dramatically. Syringes were not required in subsequent experiments. (**D**) Comparison of monolayer growth rate depending on the density at which cells are seeded in the sealed-chip. Cells were seeded at ~75x10^6 cell per mL in subsequent experiments on confluent monolayers. All scale bars are 50µm.

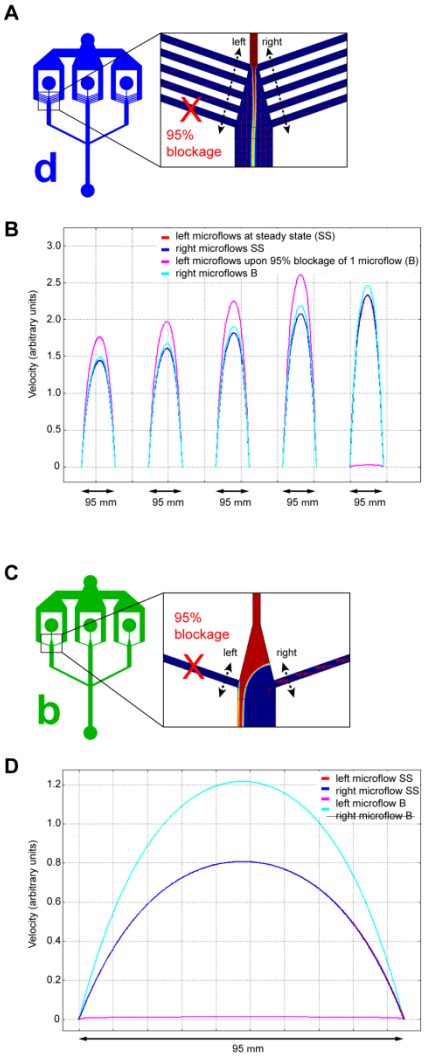

Supplementary Figure S2. Comparison of the velocity field changes in the sheath flow microchannels upon 95% blockage of a single microchannel in chips d and b. (**A**) Geometry of chip d. Sheath flows were split into multiple microflows and 95% blockage was applied to one microflow. Inset: magnified area displaying the inducer concentration profile in the main channel following blockage of one sheath microflow. High concentrations of treatment chemical appear in warm colours. (**B**) Velocity field graphs for the sheath microflows before and after blockage of the last microflow. Blockage of the left-most microflow leads to a much greater increase in velocity (thus flow rate) in the left microchannels compared to the right ones. This compensation explains the limited flow deflection (see magnified area in A). (**C**) Geometry of chip b. In contrast to chip d, only one sheath microflow is present on each side. Inset: magnified area displaying the treatment chemical concentration profile in the main channel following blockage of one sheath microflow. High concentrations of chemical inducer appear in warm colours. (**D**) Velocity field graphs for each microflow before and after blockage of the left sheath microflow. Blockage of the left microflow results in a large increase in the velocity of the right microflow, leading to a dramatic flow deflection (see magnified area in C). Comparison of A-B and C-D illustrates the robustness of flow positioning afforded by utilizing multiple sheath flows.

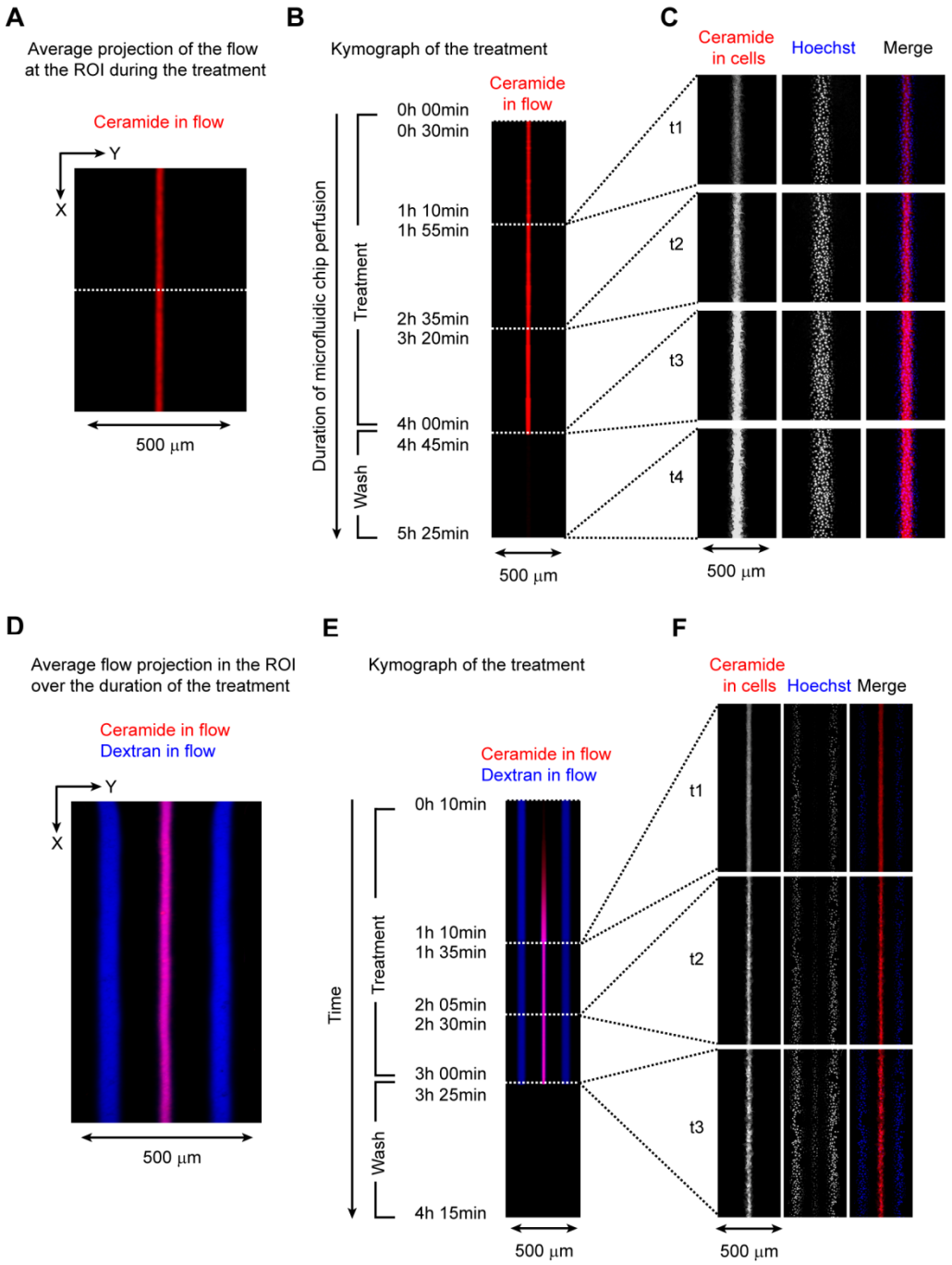

Supplementary Figure S3. Spatitemporal treatment protocol for Fig. 2A-E (S3A-C) and Fig. 3A-E (S3D-F). (**A, D**) Spatial distribution of fluorescence intensity at the ROI averaged over the duration of the treatment (4h). The line-scan intensity profile of such projections was used to determine the average treatment gradient cells were exposed to (i.e. the effective input gradient) in Fig. 3, Fig. 4 and sup Fig. S7. (**B, E**) Annotated kymograph of the treatment flow during the experiment taken along the dotted line in A. (**C, F**) Imaging of fluorescent vital dye incorporation across the monolayer at different time points during treatment. The width of Hoechst fluorescence intensity continued to increase even after cessation of treatment (compare C t3 and t4).

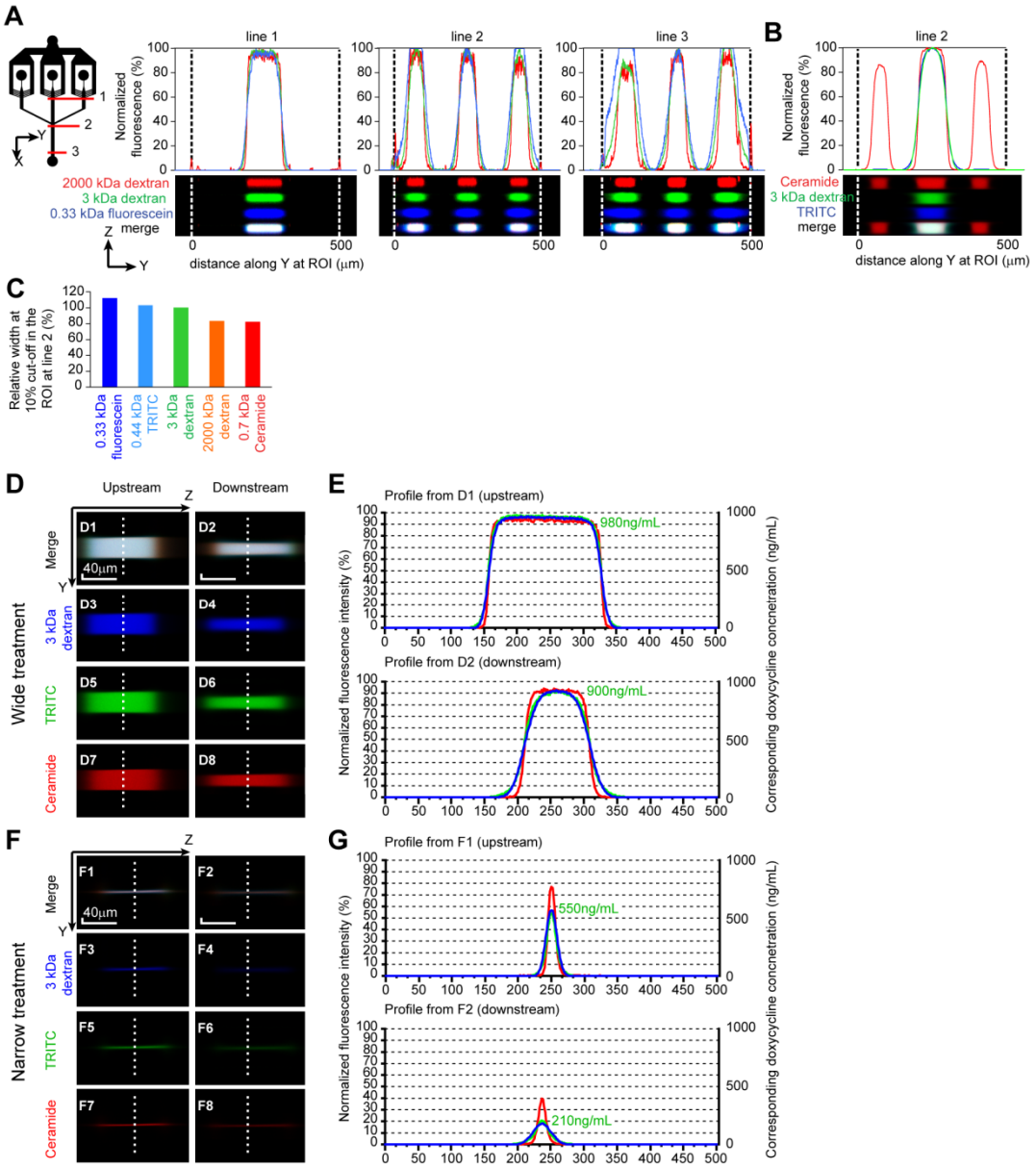

Supplementary Figure S4. Effect of lateral diffusion on gradient shapes imaged at the beginning of the treatment stream (close to the inlet) and at the ROI, for 5 dyes of different molecular weights and hydrophilicity. (**A**) Effect of lateral diffusion on various dyes along the treatment flow. Central and lateral flows are labeled with all three dyes: 0.33kDa fluorescein, 3kDa dextran and 2000kDa dextran, mixed in equimolar concentrations. Imaging at line 1 (see the chip scheme on the left) reveals little difference between the 0.33, 3 and 2000kDa dye sharp gradients, as expected for positions close to where the sheath microflows converge. Imaging at line 2 shows increased lateral spreading of the smaller dyes, which was augmented at line 3 due to further lateral diffusion, Note that this effect is more pronounced in lateral flows, for which the distance between line 1 and 2 is longer than for the central flow. (**B**) Imaging at line 2 of the central flow perfused with a solution containing ceramide, 3kDa dextran and TRITC in equimolar concentrations. Note that the ceramide gradient remains very sharp compared to 3kDa dextran and TRITC, illustrating the fact that hydrophobicity limits considerably the extent of lateral diffusion. (**C**) Expected treatment flow widths at the beginning of the ROI (line 2 in A) for various dyes, normalized to the treatment flow width expected for a 3kDa dextran treatment. Amongst hydrophilic dyes, a good agreement is found

between molecular weight and expected treatment flow width (the smaller the weight, the wider the treatment flow). In contrast, the small MW amphiphilic ceramide dye leads to the smallest a expected treatment width, perhaps due to the spontaneous formation of micelles of much higher apparent MW. (**D**) "Wide" treatment flow imaging upstream and downstream in the microchannel (corresponding to line 1 and 2, respectively, in A) along the YZ axis. (**E**) Plots of fluorescence intensities along the dotted line in D1 (top) and D2 (bottom), normalized to input fluorescence levels. Fluorescence intensity profiles in the top graph are sharp and quasi identical for all three dyes showing no sign of lateral diffusion, as expected for positions close to the zone where sheath microflow converge. In comparison in the bottom graph, fluorescence intensity profiles for 3kDa dextran and TRITC are less sharp and have spread spatially under the effect of lateral diffusion. Due to its hydrophobicity, ceramide undergoes less lateral diffusion than TRITC despite having a comparable molecular weight. (**F**) "Narrow" treatment flow imaging upstream and downstream in the microchannel (corresponding to line 1 and 2, respectively, in A) along the YZ axis (**G**) Plots of fluorescence intensities along the dotted line in F1 (top) and F2 (bottom), normalized to input fluorescence levels. Fluorescence intensity profiles in the top graph are sharp for all three dyes. However, lateral diffusion within the short distance from the inlet has been sufficient to reduce the maximum concentrations of all three dyes (down to 55% for 3kDa dextran and TRITC). In the bottom graph, maximum concentrations have been further reduced (down to 21% for TRITC and to 18% for 3kDa dextran), and the fluorescence intensity profiles for 3kDa dextran and TRITC are significantly shallower due to the effect of lateral diffusion. Thanks to its hydrophobicity, ceramide undergoes less lateral diffusion. Note that a narrow treatment imaged by TRITC (typically corresponding to a 2-4 cell-wide treatment for doxycycline) leads to a 5 fold decrease in maximum concentration at the ROI.

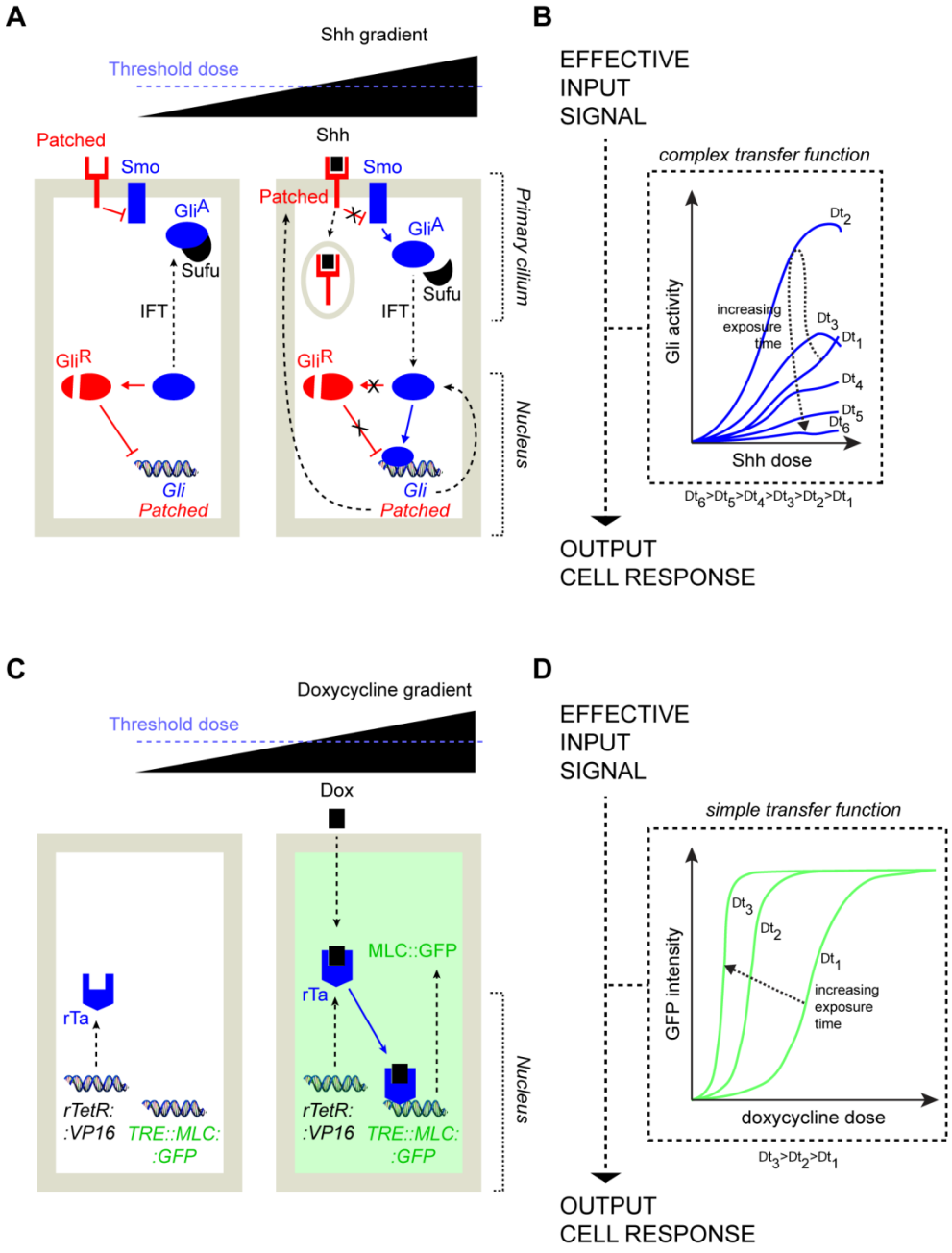

Supplementary Figure S5. Comparison of the Sonic-Hedgehog (Shh) and Tet-ON gene transcription pathways. (**A**) Simplified schematic of the gene transcription induced by the Sonic-Hedgehog (Shh) morphogenetic pathway in a target tissue. The left cell is exposed to a Shh dose below the activation threshold, where inhibition of Smoothened (Smo) by Patched leads to the transcriptional repression of Gli and Patched by the repressor form of Gli (GliR). The right cell is exposed to a Shh dose above the activation threshold. Shh binding to Patched leads to the internalization of the receptor-ligand complex, and the dysinhibition of Smo, which in turn leads to the release of active Gli (GliA) from its complex with Supressor of fused (Sufu) and to its translocation from the primary cilium (PC) to the nucleus via the intraflagellar transport machinery (IFT). GliA then activates Shh downstream target genes, including Patched and Gli itself, whose activities feedback to the transduction pathway. (**B**) Schematic plot of the relationship between Shh spatiotemporal gradient (Effective input signal) and the Gli activity (output cell response), adapted from Fig. 1C in [42]. The intricated Shh transduction pathway generates a complex time- and dose-

dependent function (in engineering terms: a transfer function, see the mathematical description proposed in [42]). (**C**) Schematic of the Tet-ON transduction pathway in our MLC-GFP MDCK II cell line. The left cell is exposed to a non-permissive dose of doxycycline. The tetracycline Receptor-VP16 transactivator (rTa) in its unbound conformation is unable to bind the tetracycline responsive element (TRE), and MLC::GFP transcription is minimal. The right cell is exposed to a permissive doxycycline dose. Doxycycline diffuses through the cell membrane to the nucleus where it binds rTa. The doxycyline-bound rTa then binds the TRE, activating MLC::GFP transcription. (**D**) Schematic plot of the relationship between doxycycline spatiotemporal gradient (Effective input signal) and the GFP intensity (output cell response). The GFP intensity is a simple function (depicted by classical sigmoidal dose-response curves) of the duration and the concentration of doxycycline exposure: longer exposures or higher concentrations lead to higher GFP levels up to a saturation level.

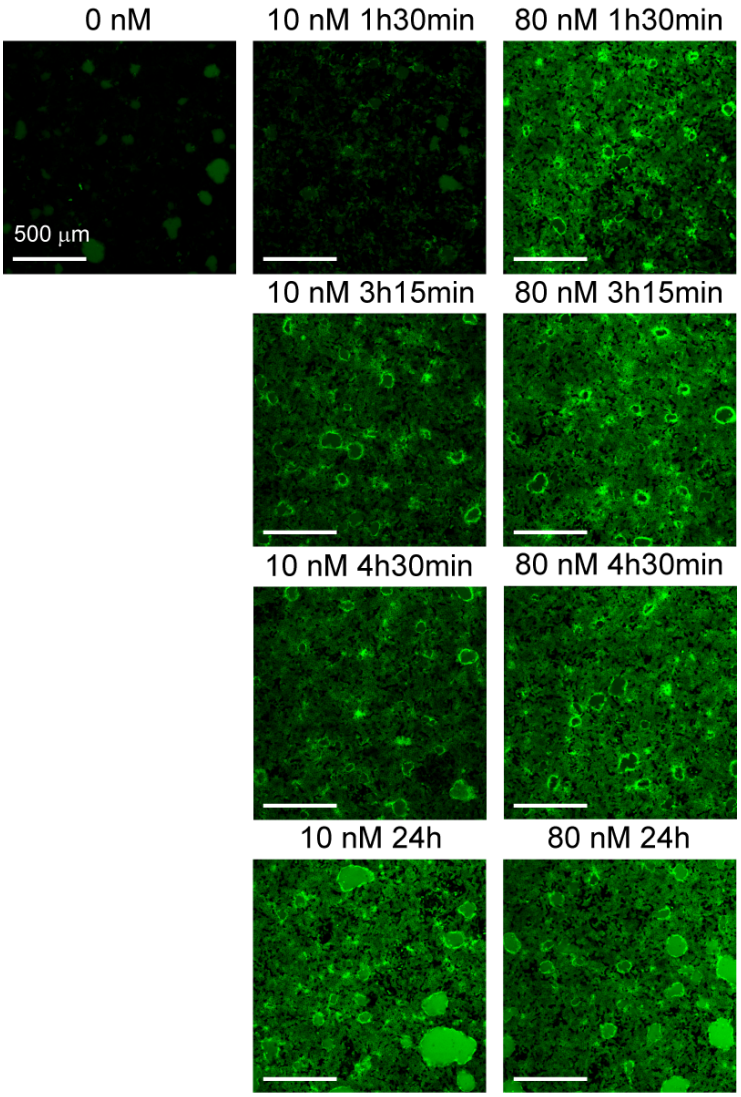

Supplementary Figure S6. Imaging of doxycycline-induced MLC::GFP expression 24h after treatments of different concentrations and durations. Each panel shows a representative image. Such images were used to derive the doxycycline/GFP dose-response curves presented in Fig. 3G. The concentration of doxycycline and duration of exposure are indicated above each panel. All panels were acquired with identical laser intensity and gain settings and are presented with identical intensity scales to allow visual comparison.

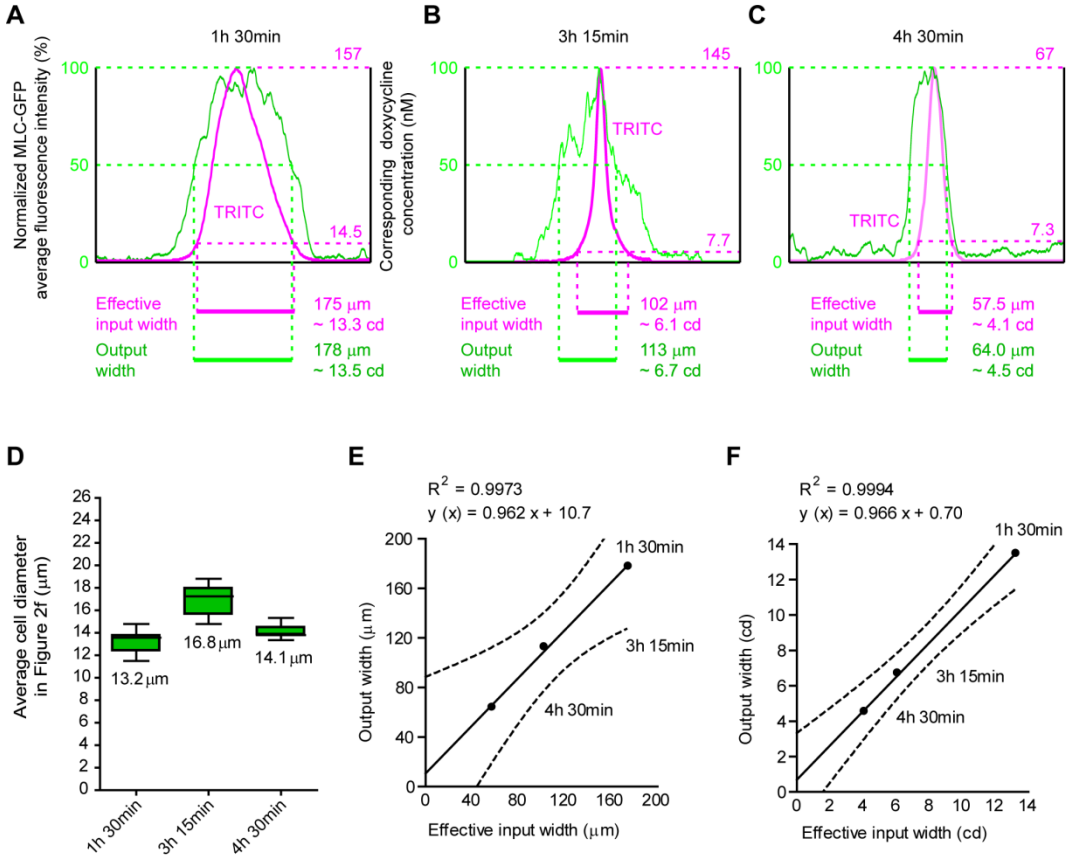

Supplementary Figure S7. Relationship between effective input width and output width in clamped chips. (**A-C**) treatment fluorescence intensity profile averaged over the duration of treatment and output MLC-GFP fluorescence intensity profile 24h after treatment. Both profiles were acquired in the ROI. Profiles are presented for acute localized doxycycline treatments with durations of 1h30min (**A**), 3h15min (**B**) and 4h30min (**C**) in clamped chips, corresponding to the images shown in Fig. 4B. Effective input widths were inferred from TRITC fluorescence profiles averaged over the duration of treatment. Activating doxycycline concentrations for each acute treatment were determined using the dose-response curves shown in Fig. 3G. (**D**) Distribution of MDCK cell diameters for the experiments presented in panels **A-C** and Fig. 4B experiments. The average cell diameter depended primarily on the compaction of the cell monolayer. (**E**) Correlation between effective input and output widths measured in microns, in clamped chips. (**F**) Correlation between effective input and output widths measured in cell diameters (cd), in clamped chips (also presented in Fig. 4C). Dotted lines denote the 95% confidence interval. The correlation between input and output width was improved when converting data to cell diameter units (compare also confidence intervals between panels **E** and **F**). This confirms that the relevant unit of input integration and cell monolayer response is the single cell.

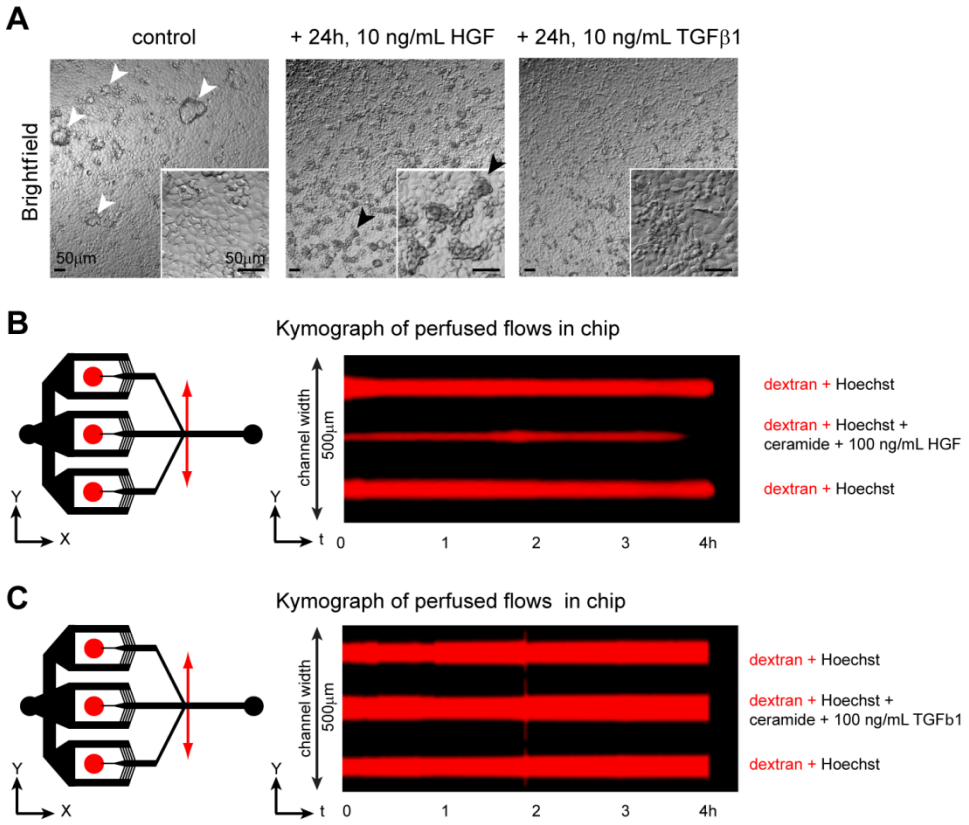

Supplementary Figure S8. HGF and TGFβ1 treatments. (**A**) Effect of global treatment with low-concentrations of HGF and TGFβ1 for 24h on confluent epithelial monolayers grown on 3D-collagen gels. Control cells often form dome-like structures (white arrowheads). 10ng/mL HGF treatment leads to the formation of large protuberances of groups of rounded cells above the cell monolayer (black arrowheads), while 10ng/mL TGFβ1 treatment leads to elongated cell shapes and single cells leaving the monolayer, either remaining attached to it or dying. (**B**) Kymograph showing the spatiotemporal treatment protocol for the experiment illustrated in figure 5A-B. (**C**) Kymograph corresponding to the experiment illustrated in figure 5H-I.

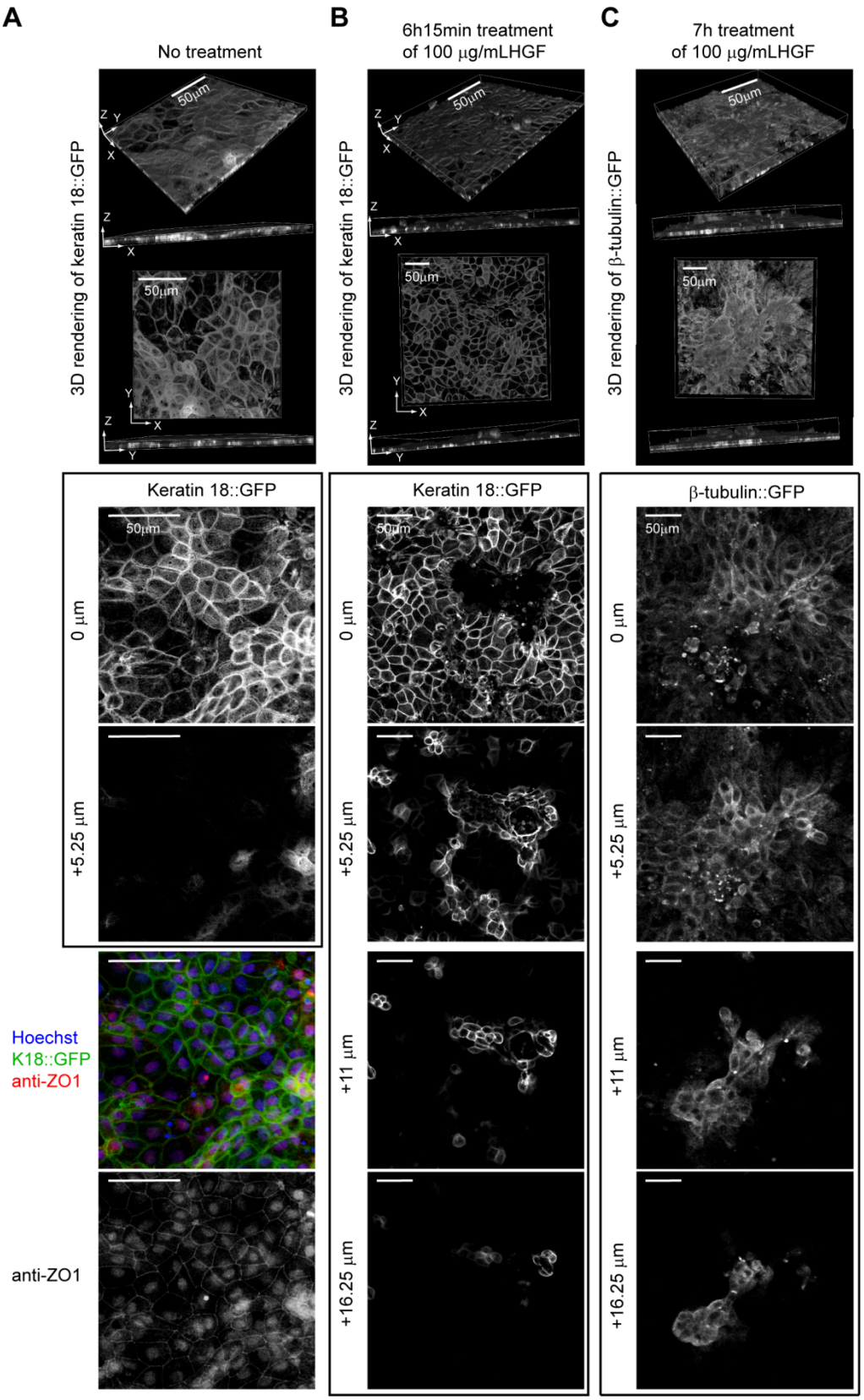

Supplementary Figure S9. Keratin18::GFP and β-tubulin::GFP are not affected by localized exposure to HGF at 24h after the onset of treatment. (**A**) Control untreated region of a monolayer expressing K18::GFP, 24h after the onset of treatment. The monolayer is flat (see 3D rendering and and confocal sections taken at 0 and +5.25 µm from the median plane of the monolayer). The anti-

ZO1 staining confirms that the monolayer possesses tight junctions and is epithelial. Note that in all experiments using anti-ZO1 antibody, aspecific nuclear staining was observed. (**B**) Exposure of K18::GFP cells to HGF leads to the creation of protuberances in the treated region. K18::GFP fluorescence intensity and localization do not seem affected by the treatment at 24h. Protruding cells extend well beyond the normal height of the monolayer as shown by confocal XY sections taken at 5.25, 11 and 16.25μm. (**C**) Exposure of β-tubulin::GFP cells to HGF leads to the creation of protuberances in the treated region. β-tubulin::GFP fluorescence intensity and localization do not seem affected by the treatment at 24h. Protruding cells extend well beyond the normal height of the monolayer as shown by confocal XY sections taken at 5.25, 11 and 16.25μm.

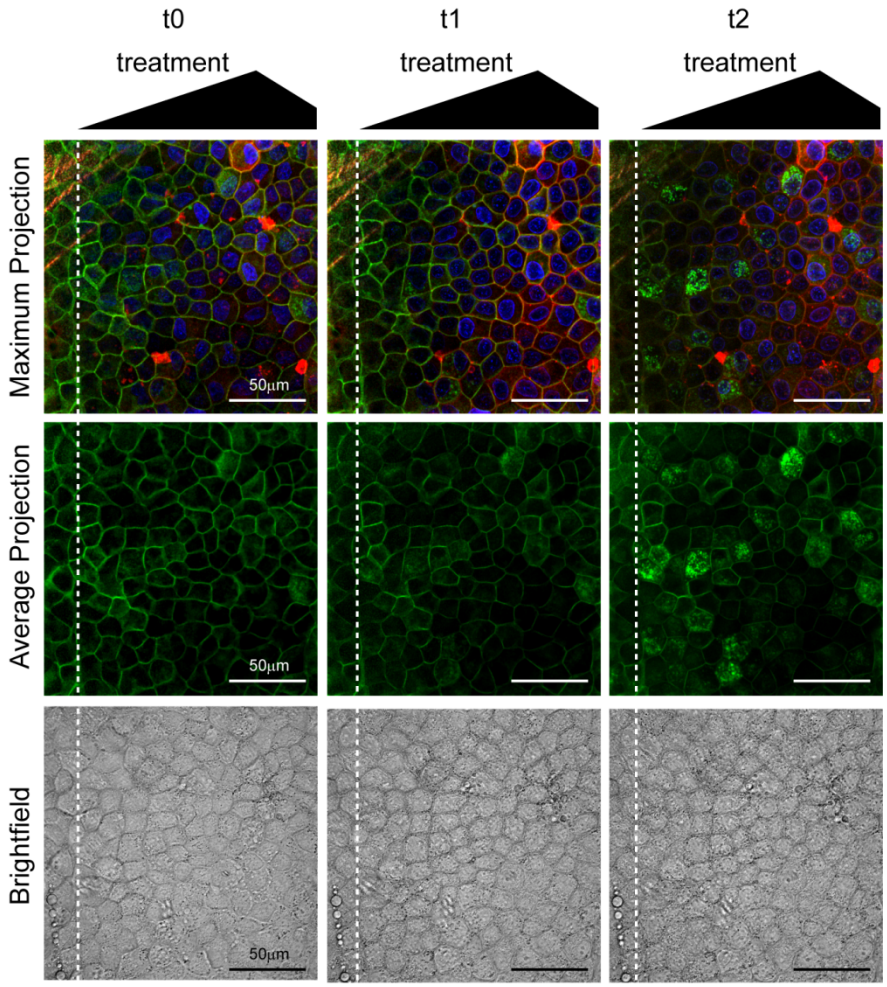

Supplementary Figure S10. Observation of E-cadherin::GFP in MDCK cells 24h after localized exposure to TGFβ1 for 4h in a clamped-chip. Upon TGFβ1 exposure, E-cadherin::GFP relocalises from intercellular junctions (t0) to the cytoplasm (t2), suggesting that TGFβ1 induces E-cadherin endocytosis as formerly described [36, 37]. t0: beginning of treatment, t1 = t0 + 1h30min, t2 = t0 + 3h. In all panels, ceramide staining is shown in red, E-cadherin-GFP localization is shown in green.